

# Octave-spanning dissipative Kerr soliton frequency combs in $\text{Si}_3\text{N}_4$ microresonators

Martin H. P. Pfeiffer<sup>1</sup>, Clemens Herkommer<sup>1,2</sup>, Junqiu Liu<sup>1</sup>, Hairun Guo<sup>1</sup>,

Maxim Karpov<sup>1</sup>, Erwan Lucas<sup>1</sup>, Michael Zervas<sup>1</sup>, Tobias J. Kippenberg<sup>1\*</sup>

1. *École Polytechnique Fédérale de Lausanne (EPFL), CH-1015 Lausanne, Switzerland and*

2. *Technische Universität München (TUM), D-80333, München, Germany*

Octave-spanning, self-referenced frequency combs are applied in diverse fields ranging from precision metrology to astrophysical spectrometer calibration. The octave-spanning optical bandwidth is typically generated through nonlinear spectral broadening of femtosecond pulsed lasers. In the past decade, Kerr frequency comb generators have emerged as novel scheme offering chip-scale integration, high repetition rate and bandwidths that are only limited by group velocity dispersion. The recent observation of Kerr frequency combs operating in the dissipative Kerr soliton (DKS) regime, along with dispersive wave formation, has provided the means for fully coherent, broadband Kerr frequency comb generation with engineered spectral envelope. Here, by carefully optimizing the photonic Damascene fabrication process, and dispersion engineering of  $\text{Si}_3\text{N}_4$  microresonators with 1 THz free spectral range, we achieve bandwidths exceeding one octave at low powers ( $\mathcal{O}(100\text{ mW})$ ) for pump lasers residing in the telecom C-band ( $1.55\text{ }\mu\text{m}$ ), as well as in the O-band ( $1.3\text{ }\mu\text{m}$ ). Precise dispersion engineering enables emission of two dispersive waves, increasing the power in the spectral ends of the comb, down to a wavelength as short as 850 nm. Equally important, we find that for THz repetition rate comb states, conventional criteria applied to identify DKS comb states fail. Investigating the coherence of generated, octave-spanning Kerr comb states we unambiguously identify DKS states using a response measurement. This allows to demonstrate octave-spanning DKS comb states at both pump laser wavelengths of  $1.3\text{ }\mu\text{m}$  and  $1.55\text{ }\mu\text{m}$  including the broadest DKS state generated to date, spanning more than 200 THz of optical bandwidth. Octave-spanning DKS frequency combs can form essential building blocks for metrology or spectroscopy, and their operation at  $1.3\text{ }\mu\text{m}$  enables applications in biological and medical imaging such as Kerr comb based optical coherence tomography or dual comb coherent anti-stokes Raman scattering.

## I. INTRODUCTION

Optical frequency combs with coherent optical bandwidths of one octave or more are required for many applications, such as precision spectroscopy [1], optical frequency synthesis [2] or astrophysical spectrometer calibration [3]. Conventionally these spectra are synthesized by nonlinear spectral broadening of a pulsed laser [1]. However, ensuring coherent spectral broadening, a smooth spectral envelope, and sufficient power in the spectral ends for a given pulse source can be challenging, in particular for high repetition rate pulse sources. Kerr frequency combs [4] have emerged as alternative scheme that enables compact form factor, high repetition rates and broadband optical frequency combs, that are even amenable to wafer-scale integration with additional electrical or optical functionality. The spectral bandwidth of Kerr frequency combs, being independent of a specific material gain and primarily determined by the resonator's group velocity dispersion (GVD), has reached octave span shortly after the principle's first demonstration [5, 6], although in the high noise operation regime [7]. Only recently, the observation of dissipative Kerr soliton (DKS) formation in microresonators has enabled the controlled excitation of fully coherent Kerr frequency combs [8].

When operated in the single soliton state, DKS fre-

quency combs feature high coherence across their bandwidth and a smooth spectral envelope that can be numerically predicted with high accuracy using the Lugiato-Lefever equation or in frequency domain via coupled mode approaches [8–10]. Furthermore, higher order GVD causes soliton Cherenkov radiation, an oscillatory tail in the temporal soliton pulse profile, corresponding to a dispersive wave (DW) in the spectral domain, which extends the spectral comb bandwidth into the normal GVD regime [11]. Soliton Cherenkov radiation in microresonators is a fully coherent process and has e.g. allowed self-referencing and stabilization without additional spectral broadening via the  $2f$ - $3f$ -method [12]. These properties have made DKS states the preferred operational low noise states [7, 13, 14] of Kerr frequency comb generation with a growing number of applications having been demonstrated, including e.g. terabit coherent communications [15], dual comb spectroscopy [16, 17] and low noise microwave generation [18]. So far DKS formation has been observed in a variety of resonator platforms [8, 18–22] among which planar silicon nitride ( $\text{Si}_3\text{N}_4$ ) waveguide resonators have gained significant attention. Allowing CMOS-compatible, wafer-scale fabrication and exhibiting low linear and nonlinear optical losses in the telecom wavelength region,  $\text{Si}_3\text{N}_4$  microresonators bear realistic potential for applications [23]. The accurate control of waveguide dimensions during microfabrication is prerequisite to precise GVD engineering and thus tailoring of the Kerr frequency comb bandwidth [10]. Dual dispersive wave emission extending the spectral bandwidth

\* tobias.kippenberg@epfl.ch

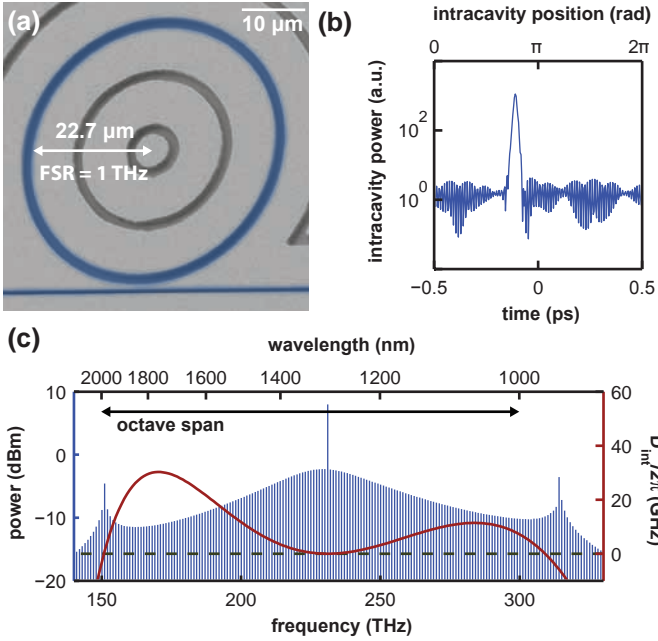


Figure 1. Octave-spanning dissipative Kerr soliton frequency comb generation in a dispersion engineered Si<sub>3</sub>N<sub>4</sub> microresonator. (a) Scanning electron microscope image of a Si<sub>3</sub>N<sub>4</sub> microresonator with 1 THz free spectral range during fabrication. The waveguide structures are highlighted in blue. (b) Simulated temporal intracavity power profile of an octave-spanning DKS frequency comb excited with 75 mW pump power for  $\kappa/2\pi = 200$  MHz using the Lugiato-Lefever equation. The two dispersive waves form an overlapping trailing and leading wave pattern. (c) The according spectral intracavity power distribution (blue) and the integrated dispersion profile  $D_{\text{int}}/2\pi$  (red) engineered for dispersive wave emission around 1  $\mu\text{m}$  and 2  $\mu\text{m}$  wavelengths.

to both sides is attractive for low power octave-spanning DKS generation but particularly challenging to realize as it requires control of higher order GVD. Most microresonators used for DKS generation to date, did not have specifically engineered GVD, resulting in limited spectral bandwidth, far below one octave.

Here we present Si<sub>3</sub>N<sub>4</sub> microresonators with a free spectral range (FSR) of 1 THz which allow for DKS frequency comb generation with bandwidths exceeding one octave. The wide FSR reduces the total power requirements to cover one octave bandwidth and benefits the nonlinear conversion efficiency in the DKS state [24]. Such microresonators are thus also of interest for wavelength regions where no high power pump sources exist. We use the recently developed photonic Damascene process [25] for wafer-scale fabrication of such high-Q microresonator devices with high yield. Figure 1(a) shows a scanning electron microscope (SEM) picture of the microresonator device including a straight bus waveguide. For small microresonator radii ( $r \approx 23 \mu\text{m}$ ) the coupling section forms a relatively large fraction of the total circumference and can cause parasitic loss. Thus, void-free fabrication of narrow coupling gaps, as provided by the

photonic Damascene process, is important. Moreover, the bus waveguide cross section needs to be engineered for high ideality coupling [26]. The fundamental mode families of the microresonator devices used in this work have a typical internal linewidth of  $\kappa_0/2\pi = 100$  MHz and thus a loaded finesse of  $\mathcal{F} \approx 10^4$  at critical coupling.

While a high microresonator finesse is beneficial to lower the power threshold of Kerr comb generation, the microresonator GVD determines mostly the power requirements to reach a certain spectral bandwidth. Microresonator GVD is conveniently expressed in its integrated form around a central pump frequency  $\omega_0$ :

$$D_{\text{int}}(\mu) \equiv \omega_\mu - (\omega_0 - D_1\mu) = \frac{D_2\mu^2}{2!} + \frac{D_3\mu^3}{3!} + \dots$$

$D_{\text{int}}(\mu)$  is the resonance frequency deviation of the  $\mu$ -th mode  $\omega_\mu$  relative to the central pump mode  $\omega_0$  from the equidistant grid defined by the repetition rate  $D_1/2\pi$ . DKS formation requires anomalous GVD ( $D_2 > 0$ ) as the associated resonance frequency deviation is compensated by the nonlinear phase shift induced by the soliton. In the case of dominant quadratic GVD, the 3 dB bandwidth of the resulting characteristic  $\text{sech}^2$  soliton spectral envelope, and thus the temporal pulse width, is a function of the cavity detuning and  $D_2$  [8]. Low positive values of  $D_2$  result in larger optical bandwidths for a given pump power and detuning. Beyond this, dispersive wave formation offers an effective way to coherently enlarge the bandwidth into the normal GVD with locally enhanced comb tooth power in the spectral ends [19, 27]. Dispersive waves are emitted in resonances which are phase matched by the soliton induced nonlinear phase shift and the spectral positions of DWs are thus approximately given by the linear phase matching criterion  $D_{\text{int}} = 0$ . For dominant, negative fourth-order dispersion  $D_4$  two DW positions can be engineered, causing dual dispersive wave emission.

We design the microresonator waveguide cross section based on finite element (FEM) simulations of the resonator's TE<sub>00</sub> mode family dispersion. Dispersive wave formation is engineered to occur around wavelengths of 1  $\mu\text{m}$  and 2  $\mu\text{m}$  spanning an octave bandwidth around the pump line at 1.3  $\mu\text{m}$  or 1.55  $\mu\text{m}$ . Full 3D finite difference time domain simulations are employed to engineer the bus waveguide cross section for high ideality coupling to the TE<sub>00</sub> mode family [26]. Next, we simulate the octave-spanning DKS generation using a Lugiato-Lefever model [9, 28] for a critically coupled Si<sub>3</sub>N<sub>4</sub> microresonator with linewidth  $\kappa/2\pi = 200$  MHz driven by a pump laser of 75 mW power. Figure 1(b), (c) show the intracavity field and the spectral envelope of the simulated single DKS state. As can be seen the two dispersive waves are present in the temporal intracavity field as trailing and following wave patterns which fill the complete cavity. Furthermore, close examination reveals that the position of the higher frequency dispersive wave is slightly offset from the linear phase-matching point, indicating the approximative nature of the criterion  $D_{\text{int}}(\mu) = 0$ .

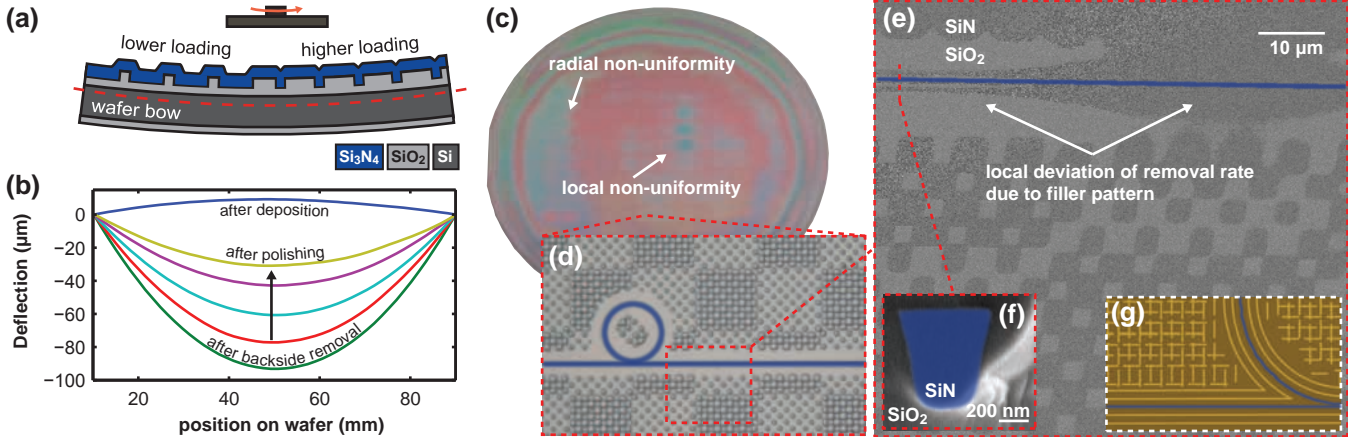


Figure 2. Origins of non-uniform planarization in the photonic Damascene process. (a) Schematic representation of wafer bow and local loading causing non-uniformity during chemical mechanical planarization. (b) Measurement of wafer bow evolution during planarization for a 525  $\mu\text{m}$  thick 4" wafer with  $\sim 1 \mu\text{m}$  thick  $\text{Si}_3\text{N}_4$  thin film. (c) Photograph of a 4" wafer after planarization showing non-uniformity through colored interference patterns. (d) Optical microscope image of a 1 THz FSR microresonator surrounded by a "checkerboard" filler pattern. The  $\text{Si}_3\text{N}_4$  waveguides are highlighted in blue. (e) SEM image of a non-uniformly planarized bus waveguide (indicated in blue). The neighboring filler pattern patches have different loading and thus cause more  $\text{Si}_3\text{N}_4$  (dark shaded areas) to remain over the bus waveguide in certain areas. (f) Cross section of the bus waveguide used to couple light in a 1 THz FSR microresonator. The dimensions (0.5  $\mu\text{m} \times 0.67 \mu\text{m}$ ) are chosen to provide high ideality coupling to the microresonator's fundamental  $\text{TE}_{00}$  mode family. (g) Optical microscope image of waveguide structures surrounded by optimized filler pattern.

In the following, we first discuss the challenges of precise waveguide dimension control using the photonic Damascene process. Leveraging optimized fabrication procedures, we achieve control over the dispersive wave positions resulting in octave-spanning comb generation based on 1.3  $\mu\text{m}$  and 1.55  $\mu\text{m}$  pump lasers. The coherence of the generated Kerr frequency combs is studied and a response measurement is used to unambiguously identify DKS formation. Finally, we study octave-spanning single DKS formation for 1.3  $\mu\text{m}$  and 1.55  $\mu\text{m}$  pump wavelengths featuring the *broadest* Kerr soliton frequency comb generated to date, exceeding 200 THz in bandwidth.

## II. PRECISION DISPERSION ENGINEERING USING THE PHOTONIC DAMASCENE PROCESS

Dispersion engineering for octave-spanning Kerr frequency comb generation requires stringent waveguide width and height control on the order of 10 nm, that is challenging to meet. As detailed below via simulations (shown in Figure 3), especially the position of the dispersive wave features is very sensitive to variations of the waveguide dimensions. Although DKS frequency comb generators have been fabricated using conventional subtractive processing, several challenges arise for the fabrication of high confinement  $\text{Si}_3\text{N}_4$  waveguides for non-linear applications. In particular, these are cracking of the highly stressed  $\text{Si}_3\text{N}_4$  thin film and void formation at the microresonator coupling gap [25]. The recently

reported photonic Damascene process, employed in the present work, solves these problems by depositing the  $\text{Si}_3\text{N}_4$  thin film on a prestructured substrate and subsequent removal of the excess material using chemical mechanical planarization (CMP). A dense filler pattern surrounding the waveguide structures effectively lowers the thin film's tensile stress and enables crack free fabrication even for micron thick waveguides. Moreover, the filler pattern helps to control and unify the material removal rate across the wafer during CMP.

Although the level of control on the waveguide width is similar for Damascene and subtractive processing schemes (both relying on the precision of lithography and etching processes) the waveguide height control is substantially eased in the subtractive fabrication scheme: a typical thin film deposition non-uniformity of 3% across a 4" wafer results in a maximal 25 nm height deviation for 800 nm thick  $\text{Si}_3\text{N}_4$  waveguides. For the Damascene process the variation of the final waveguide thickness depends on the uniformity of the dry etch process used to structure the waveguide trenches and most importantly on the uniformity of the CMP process. While optical interferometry can give precise local information on the removal rate during CMP, especially the wafer bow and the local loading lead to height variations (see Figure 2(a)). This reduces the yield of devices with dimensions within the tolerance range for octave-spanning Kerr comb generation, and causes uncontrolled spectral positions of the dispersive waves.

Figure 2(b) shows the evolution of the bow during planarization of a 525  $\mu\text{m}$  thick 4" wafer measured using a thin film stress measurement tool. After deposition, the

continuous  $\text{Si}_3\text{N}_4$  film on the wafer backside causes a positive deflection as its tensile stress is higher than the stress on the wafer front side which is reduced by the prestructured surface. The removal of the backside  $\text{Si}_3\text{N}_4$  prior to the CMP inverts the bow to more than  $-90\text{ }\mu\text{m}$ . The subsequent planarization step removes the excess  $\text{Si}_3\text{N}_4$  on the front side and continuously relaxes the wafer bow. This bow variation leads to non-uniformity with radial symmetry visible as the colored interference ring pattern in Figure 2(c). Furthermore, local non-uniformity in the central wafer region can also be observed, which originates from different removal rates due to loading variations. Loading refers here to the amount of excess  $\text{Si}_3\text{N}_4$  that is in direct contact with the polishing pad and depends on the local structure density. Such local variations can also occur on much smaller scales. This is exemplified in Figure 2(e) for an area around a bus waveguide (indicated in blue) after CMP. Depending on the loading of the neighboring filler pattern, more or less  $\text{Si}_3\text{N}_4$  (darker shaded area) is remaining above the silicon dioxide ( $\text{SiO}_2$ ) preform (lighter shaded area). Such loading dependent non-uniformity leads to local variations of the waveguide height, and therefore needs to be minimized. Finally, during landing when most excess  $\text{Si}_3\text{N}_4$  is removed and mostly the  $\text{SiO}_2$  preform is in contact with the polishing pad, the material removal rate can drastically change. Thus, the polishing endpoint is hard to predict and the overall mean waveguide height differs from the target value.

Here we apply an optimized CMP process that uses higher pressure to equalize the wafer bow and a thicker wafer substrate ( $700\text{ }\mu\text{m}$ ) that reduces the amount of initial wafer bow to  $-50\text{ }\mu\text{m}$ . The removal rates for  $\text{Si}_3\text{N}_4$  and  $\text{SiO}_2$  are chosen to be similar, limiting the uncertainty during landing. In order to reduce local loading effects, a novel filler pattern (see Figure 2(g)) is used which homogenizes the loading while providing sufficient stress release for crack-free fabrication. The dispersion control achieved using this optimized CMP process is summarized in Figure 3. Based on FEM simulations of microresonator GVD shown in Figure 3(a), the target waveguide height of  $0.74\text{ }\mu\text{m}$  was chosen to enable octave-spanning DKS frequency comb generation in the resonator's  $\text{TE}_{00}$  mode family for a  $1.3\text{ }\mu\text{m}$  pump laser. The simulation predicts dispersive wave formation around  $1\text{ }\mu\text{m}$  and  $2\text{ }\mu\text{m}$  for a  $1.425\text{ }\mu\text{m}$  wide, fully  $\text{SiO}_2$  cladded waveguide with  $82^\circ$  sidewall angle. As shown in Figure 3(a), a waveguide height deviation of only  $10\text{ nm}$  causes a shift of the low frequency dispersive wave position by  $5\text{ THz}$  (i.e. ca.  $\Delta\lambda = 100\text{ nm}$  in wavelength). A change in the waveguide width does not strongly influence the position of the low frequency dispersive wave but changes the position of the high frequency dispersive wave.

The dispersion of different samples is evaluated based on the spectral envelopes of the generated frequency combs. The low values of microresonator GVD (i.e.  $D_2/2\pi \sim \mathcal{O}(20\text{ MHz})$ ) and the bandwidth limitations of our precision diode laser spectroscopy setup [29], did not

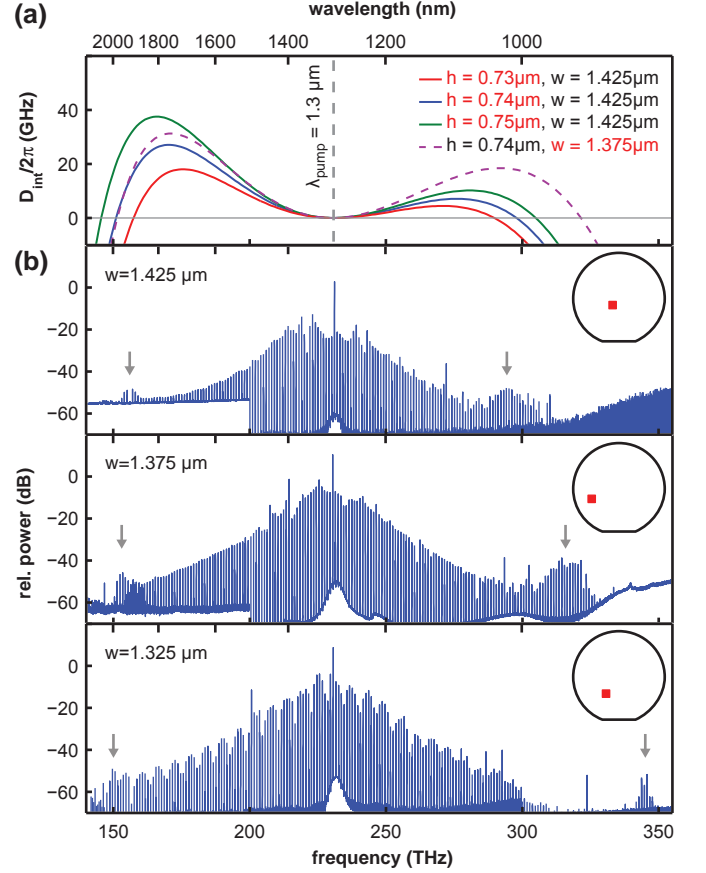


Figure 3. Wafer-scale dispersion engineering of octave-spanning Kerr frequency combs. (a) Simulated integrated dispersion  $D_{\text{int}}(\nu)/2\pi$  of fully cladded  $\text{Si}_3\text{N}_4$  microresonators with  $82^\circ$  sidewall angle and different widths and heights for generating dual dispersive wave DKS states. For a pump wavelength of  $1.3\text{ }\mu\text{m}$  dispersive waves can be excited in a linear approximation at positions close to the zero-points of the integrated dispersion. (b) Unstable modulation instability, high-noise Kerr frequency combs generated in three different samples fabricated on the same wafer at different positions which are indicated in the inset. The spectral position of the two dispersive waves are indicated by gray arrows. The samples have by design a difference of  $50\text{ nm}$  in waveguide width which enables tuning of the high frequency dispersive wave position, demonstrating the excellent dimension control of the Damascene process.

allow to measure higher order dispersion terms. Figure 4(a) shows the setup used for DKS frequency comb generation. A  $1.3\text{ }\mu\text{m}$  external cavity diode laser (ECDL) is amplified using a tapered semiconductor amplifier (SOA) to a maximum power of  $0.75\text{ W}$ . Laser light is coupled into the photonic chip using lensed fibers and inverse tapered waveguides with about  $\sim 3\text{ dB}$  loss per facet. During the laser tuning into the  $\text{TE}_{00}$  mode family resonance, the transmission through the device as well as the generated comb light are recorded using photodiodes ( $f_{3\text{dB}} = 1\text{ GHz}$ ). Up to three optical spectrum analyzers (OSA) are used to capture the generated broadband

comb spectra. Figure 3(b) shows octave spanning unstable modulation instability (uMI) comb states excited in three different microresonator chips. The sample position on the 4" wafer is provided as inset. As can be seen, the position variation of the low frequency dispersive wave for the three samples is 5.5 THz around the designed target value of 150 THz. In comparison with the simulations in Figure 3(a) this indicates a variation of less than  $\pm 10$  nm in waveguide height around the target value of  $0.74 \mu\text{m}$ . Moreover, the width variation allows the position of the high frequency dispersive wave to be tuned. A waveguide width reduction of 50 nm in the design moves the position of the high frequency dispersive wave by  $\sim 25$  THz in good agreement with simulations. These measurements reveal *actual* lithographic control over the dispersive wave position, rather than post fabrication selection. The photonic Damascene process with optimized planarization step thus offers sufficient precision in the control over waveguide dimensions to allow for wafer-scale fabrication of microresonators with engineered dispersion properties over a full octave of bandwidth.

### III. COHERENCE AND SOLITON IDENTIFICATION

For applications of the octave-spanning Kerr comb state coherence is a key requirement. Common methods to classify the coherence of Kerr comb states are the measurements of the low frequency amplitude noise of the generated comb light, the repetition rate beat-note, as well as heterodyne beat-notes with reference lasers [7]. Among the different low noise comb states [7, 13, 14], the DKS state is particularly attractive as it provides high coherence across its entire bandwidth. Soliton Kerr comb states have in particular been identified via the characteristic transmission steps in the generated comb light, via the red-detuned nature of the pump laser, as well as the characteristic soliton spectral envelope. Although the spectra contain no direct information on coherence, for microresonators with dominant (positive) quadratic dispersion  $D_2$  the single soliton state exhibits a characteristic spectral  $\text{sech}^2$  envelope. For broadband Kerr combs the spectral envelope can exhibit dispersive waves, due to higher order microresonator dispersion. Although dispersive wave features are also present in the uMI state spectra, in the DKS state their width reduces with a simultaneous increase in the individual comb tooth power and a shift of the dispersive wave maximum [19]. Other spectral signatures of the DKS regime include the soliton Raman self-frequency shift, that leads to a redshift of the soliton's  $\text{sech}^2$  envelope with respect to the pump [30]. The Raman self-frequency shift is absent in the uMI comb state, but can be masked in the DKS state by the soliton recoil due to dispersive wave formation. For octave spanning soliton Kerr combs with THz mode spacing and dispersive wave emission due to microresonator GVD

and avoided modal crossings [31], DKS state identification purely based on the spectral envelope is unreliable.

In contrast, a recently introduced response measurement technique [32] allows to unambiguously identify DKS comb states, and is applied here for the first time to octave spanning soliton states. Figure 4(a) shows the setup used to investigate the coherence of comb states generated with a  $1.3 \mu\text{m}$  and  $1.55 \mu\text{m}$  ECDL. The  $1.55 \mu\text{m}$  ECDL is amplified using an erbium-doped fiber amplifier (EDFA) and in order to perform the response measurement, a phase modulator with 10 GHz bandwidth is added before the amplifier. A vector network analyzer (VNA), probing the Kerr comb state's response, drives the EOM and receives the signal via a photodiode with 25 GHz bandwidth. We note that this measurement was only possible using the  $1.55 \mu\text{m}$  pump laser due to the lack of an appropriate phase modulator for the  $1.3 \mu\text{m}$  pump path. A heterodyne beat note of the comb with a fiber laser at 1064 nm is recorded using an electrical spectrum analyzer (ESA). All presented Kerr frequency comb states are excited using a simple laser tuning method, applying a linear voltage ramp provided by an arbitrary function generator (AFG) to controllably tune into a comb state [8, 32].

DKS formation is accompanied by characteristic step features that occur simultaneously in the generated comb and transmitted light trace [8]. However, in the experiments reported here in Figure 4(b)-(d), we found that abrupt changes in the transmitted power do *not* necessarily originate from soliton formation. Instead, abrupt changes between different non-solitonic comb states, as well as resonance splitting due to waveguide surface roughness or near-by resonances of other mode families can cause similar features. Figure 4(b) shows the optical spectrum of a comb state generated by tuning the  $1.3 \mu\text{m}$  pump laser with  $P_{\text{bus}} = 125 \text{ mW}$  in the bus waveguide into the step feature visible in Figure 4(d). The spectrum spans an octave and is highly structured, featuring individual sharp lines at the dispersive wave positions. Moreover, the beat-note of an individual comb tooth with a fiber laser at 1064 nm (see Figure 4(e)) shows low noise characteristics i.e.  $> 20$  dB signal-to-noise ratio in a 100 kHz resolution bandwidth (RBW). Based on these measurements, the generated comb state would agree with properties associated with a multi-soliton state. However, close examination of the generated spectral lines, shown in Figure 4(c), reveals that certain comb lines have a splitting of  $\sim 8$  GHz, *incompatible* with a DKS comb state and associated with merging of individual *subcombs* [7]. Importantly, commonly employed [7, 33] low frequency amplitude noise measurements, and even local heterodyne beat-note measurements, are insufficient discriminators, unless they are performed over sufficiently wide bandwidth to detect the subcomb spacing (here  $\gg 1$  GHz). Indeed, for the measurements above, no noise  $< 1$  GHz is observed, which would lead to an erroneous soliton state identification.

A more reliable method is using the response of the

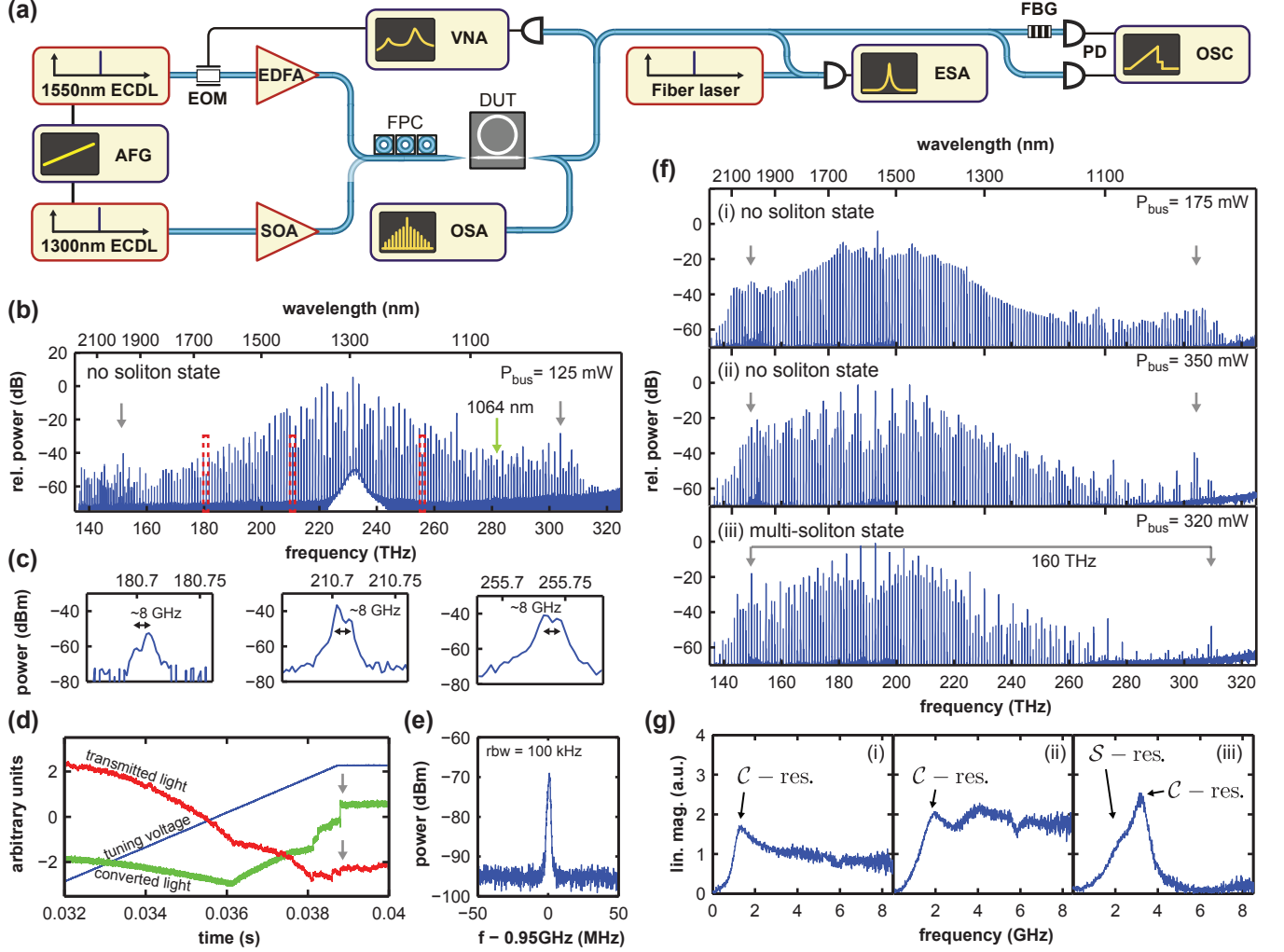


Figure 4. Distinction of octave-spanning multi-soliton states and non-solitonic states. (a) Schematic of the setup used to generate octave-spanning Kerr combs using 1.3  $\mu\text{m}$  or 1.55  $\mu\text{m}$  pump lasers. In both cases an arbitrary waveform generator (AFG) provides the voltage ramp to tune the external cavity diode seed laser (ECDL) into a resonance of the device under test (DUT). Either an erbium-doped fiber amplifier (EDFA) or a semiconductor tapered amplifier (SOA) is used to amplify the seed laser before coupling onto the photonic chip using lensed fibers. An oscilloscope (OSC) records the transmitted and converted comb light power during the scan. Several optical spectrum analyzers (OSA) are used to capture the full spectra of the excited comb state. A 1064nm fiber laser allows the recording of heterodyne beat-notes using a fast photodiode and an electrical spectrum analyzer (ESA). The comb state response is measured by a vector network analyzer (VNA) that drives an electro-optic phase modulator (EOM) and receives part of the transmitted light on a photodiode with 25 GHz bandwidth. (b) Highly structured octave-spanning comb state excited by tuning the 1.3  $\mu\text{m}$  pump laser into the step-like feature (which, importantly, does not originate from soliton formation) highlighted in (d) with gray arrows. The red boxes mark comb teeth which reveal a splitting of  $\sim 8$  GHz upon close examination in (c), demonstrating subcomb formation. (d) Oscilloscope trace of the voltage ramp (blue), the generated comb light (green) and the transmitted light signal (red) (e) Narrow heterodyne beat note of a 1064nm fiber laser with the comb tooth marked with a green arrow in (b) of a non-solitonic comb state. (f) Three comb states excited in three different microresonators with the same waveguide dimensions. (g) Response measurements associated with the comb states in (f). The position of the cavity (C-res.) and the soliton (S-res.) resonance is indicated.

comb state to a phase modulation of the pump laser. It was shown that the phase modulation response function of DKS states consists of two characteristic resonances originating from the circulating soliton pulses (S-resonance) and the cavity response (C-resonance) [32, 34]. Furthermore, the measurement allows to infer the effective pump laser detuning within the DKS state, an

important quantity determining the soliton properties. Figure 4(f) shows three comb states recorded from three microresonators on the same photonic chip having the same waveguide dimensions but varying bus-resonator distances. Again, the microresonator dispersion was designed for dispersive wave emission around 1  $\mu\text{m}$  and 2  $\mu\text{m}$ , here upon pumping with a 1.55  $\mu\text{m}$  laser. We ex-

cite different comb states and analyze their corresponding response functions shown in Figure 4(g). State (i) is a uMI state and the response function exhibits a single peak and a non-zero background noise at high frequencies. State (ii) has a much more structured spectral envelope and a seemingly sharp dispersive wave feature compared to state (i). However, the response measurement reveals a fundamentally different response than expected for a DKS state. Also, state (iii) has a strongly structured spectral envelope with similarities to the envelope of state (ii) but its response function shows two overlapping resonances. The lower frequency  $\mathcal{S}$ -resonance originates from the circulating soliton pulses and has a reduced amplitude compared to the cavity  $\mathcal{C}$ -resonance at higher frequency, whose frequency indicates the detuning. Moreover, the separation of both peaks diminishes upon laser blue detuning and increases for red detuning, respectively. We thus identify state (iii) as a multi-soliton state. The multi-soliton state leads to an increased conversion efficiency compared to the single soliton case, resulting in negligible residual pump power in the present case. Moreover, we observe a notable shift of the high frequency dispersive wave peak position (indicated by gray arrows).

#### IV. OCTAVE SPANNING SPECTRA VIA SINGLE SOLITON GENERATION

Once excited, a multi-soliton state can often be converted into a single soliton state by soliton switching upon “backward tuning” of the pump laser [32]. Figure 5 shows two examples of octave-spanning single soliton generation obtained via this technique using  $1.3\,\mu\text{m}$  or  $1.55\,\mu\text{m}$  pump lasers. We note that not all multi-soliton states excited were observed to switch to a lower soliton number upon backward tuning, but some changed into non-solitonic states. Moreover, it is observed that both single soliton combs are excited in direct vicinity of an avoided modal crossing causing strong local deviations from the characteristic  $\text{sech}^2$  shaped spectral envelope [35].

The soliton spectrum shown in Figure 5(a) features no dispersive waves indicating a dominant quadratic factor of the anomalous GVD. The response measurement shown in the inset shows a double resonance signature and reveals a cavity detuning of  $\sim 4.5\,\text{GHz}$ . The pump power is increased to  $455\,\text{mW}$  in the bus waveguide while maintaining the single DKS state, which allows for a larger soliton existence range and octave bandwidth at a cavity detuning of  $\sim 7\,\text{GHz}$ . This cavity detuning is significantly higher than previously published values for  $\text{Si}_3\text{N}_4$  microresonators indicating a strong nonlinear phase shift due to the high peak intensity of the soliton pulse [32]. The spectral envelope is fitted using a  $\text{sech}^2$  shape and a 3 dB bandwidth of  $24.85\,\text{THz}$  is extracted, corresponding to a  $12.7\,\text{fs}$  pulse. In Figure 5(b) we present the *broadest* single DKS comb state published

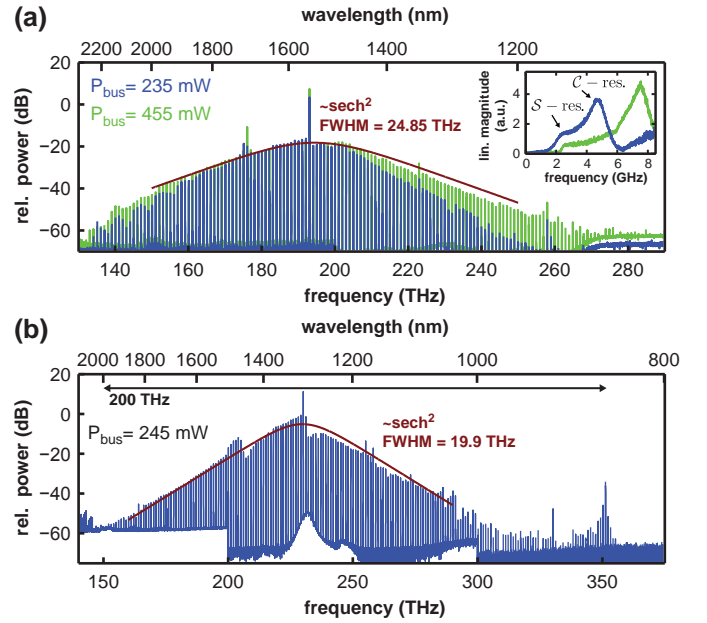


Figure 5. Octave-spanning single soliton generation at  $1.55\,\mu\text{m}$  and  $1.3\,\mu\text{m}$  pump wavelength. (a) The same single DKS state shown for two different pump laser powers and cavity detunings. Inset: Response measurement of the single DKS states shown in (a) revealing the respective pump laser cavity detuning. The  $\mathcal{S}$ - and  $\mathcal{C}$ -resonances are separated by  $\sim 2.5\,\text{GHz}$  and  $\sim 5\,\text{GHz}$ , respectively. (b) Single DKS spanning  $200\,\text{THz}$  in optical bandwidth with a dispersive wave at  $850\,\text{nm}$  excited using a  $1.3\,\mu\text{m}$  pump laser. Fits of both states with a spectral  $\text{sech}^2$  envelope are shown in red. Pump powers in the bus waveguide and fitted spectral bandwidths are noted.

to date, to the best of our knowledge. The DKS comb spans a total bandwidth of  $\sim 200\,\text{THz}$  using a pump laser at  $1.3\,\mu\text{m}$  providing only  $245\,\text{mW}$  power in the bus waveguide. The fitted 3 dB bandwidth of  $19.9\,\text{THz}$  is similar to the value of the single DKS state shown in Figure 5(a) even though the required pump power is significantly lower. This demonstrates the strong influence of dispersion on the power requirements for broadband comb generation and underlines the necessity for precise dispersion control.

#### V. CONCLUSION

In conclusion, we have demonstrated DKS generation in  $\text{Si}_3\text{N}_4$  microresonators with  $1\,\text{THz}$  FSR and spectral bandwidths exceeding one octave, both at  $1.55\,\mu\text{m}$  and  $1.3\,\mu\text{m}$  pump wavelength. The photonic Damascene process with optimized planarization step allows for high yield, wafer-scale fabrication of microresonators with precisely controlled dispersive wave positions. Our work moreover revealed that for comb states generated in  $\text{Si}_3\text{N}_4$  microresonators with  $1\,\text{THz}$  FSR, conventional criteria of coherence can fail. We carefully investi-

gated the coherence of generated comb states and unambiguously identified octave-spanning multi-DKS states based on their unique phase modulation response signature. Finally, we demonstrated single soliton generation with record bandwidth of 200 THz generated with only 245 mW of pump power.

Our findings demonstrate the technological readiness of the photonic Damascene process and integrated  $\text{Si}_3\text{N}_4$  frequency comb generators for a wide range of applications. The ability to generate ultra-short pulses also with a  $1.3\text{ }\mu\text{m}$  pump laser, as demonstrated here, opens up applications in biological and medical imaging as this wavelength represents a compromise between low tissue scattering and absorption due to water. Moreover, such DKS frequency combs with designed spectral envelopes may in the future enable chip integration and miniaturization of self-referenced frequency combs [36] and dual comb CARS [37].

### Acknowledgements

$\text{Si}_3\text{N}_4$  microresonator samples were fabricated in the Center of MicroNanoTechnology (CMi) at EPFL.

This publication was supported by Contract HR0011-15-C-0055 from the Defense Advanced Research Projects Agency (DARPA), Defense Sciences Office (DSO), funding from Air Force Office of Scientific Research, Air Force Material Command, USAF under Award No. FA9550-15-1-0099, the European Union's Horizon 2020 research and innovation programme under MIRCOMB: Marie Skłodowska-Curie IF grant agreement No. 709249 and the Swiss National Science Foundation under grant agreement No.161573 and 163864. M.K. acknowledges the support from the Marie Curie Initial Training Network FACT.

This research was carried out concurrently with the work from K. S. at NIST in the framework of the project DODOS that is available online under [33] and also reports octave spanning Kerr soliton combs with dual dispersive waves.

- 
- [1] T. Udem, R. Holzwarth, and T. W. Hänsch, *Nature* **416**, 233 (2002).
  - [2] R. Holzwarth, T. Udem, T. W. Hänsch, J. Knight, W. J. Wadsworth, and P. Russell, *Physical Review Letters* **85**, 2264 (2000).
  - [3] T. Steinmetz, T. Wilken, C. Araujo-Hauck, R. Holzwarth, T. W. Hänsch, L. Pasquini, A. Manescau, S. D'Odorico, M. T. Murphy, T. Kentischer, W. Schmidt, and T. Udem, *Science* **321**, 1335 (2008), arXiv:0809.1663.
  - [4] P. Del'Haye, A. Schliesser, O. Arcizet, T. Wilken, R. Holzwarth, and T. J. Kippenberg, *Nature* **450**, 1214 (2007).
  - [5] P. Del'Haye, T. Herr, E. Gavartin, M. L. Gorodetsky, R. Holzwarth, and T. J. Kippenberg, *Physical Review Letters* **107**, 063901 (2011).
  - [6] Y. Okawachi, K. Saha, J. S. Levy, Y. H. Wen, M. Lipson, and A. L. Gaeta, *Optics Letters* **36**, 3398 (2011).
  - [7] T. Herr, K. Hartinger, J. Riemensberger, C. Y. Wang, E. Gavartin, R. Holzwarth, M. L. Gorodetsky, and T. J. Kippenberg, *Nature Photonics* **6**, 480 (2012).
  - [8] T. Herr, V. Brasch, J. D. Jost, C. Y. Wang, N. M. Kondratiev, M. L. Gorodetsky, and T. J. Kippenberg, *Nature Photonics* **8**, 145 (2014), arXiv:1211.0733.
  - [9] S. Coen, H. G. Randle, T. Sylvestre, and M. Erkintalo, *Optics Letters* **38**, 37 (2013), arXiv:1211.1697.
  - [10] Y. Okawachi, M. R. E. Lamont, K. Luke, D. O. Carvalho, M. Yu, M. Lipson, and A. L. Gaeta, *Optics Letters* **39**, 3535 (2014), arXiv:arXiv:1307.1037.
  - [11] N. Akhmediev and M. Karlsson, *Physical Review A* **51**, 2602 (1995).
  - [12] V. Brasch, E. Lucas, J. D. Jost, M. Geiselmann, and T. J. Kippenberg, *Light: Science & Applications* **6**, 1 (2017), arXiv:1605.02801.
  - [13] X. Xue, Y. Xuan, Y. Liu, P.-H. Wang, S. Chen, J. Wang, D. E. Leaird, M. Qi, and A. M. Weiner, *Nature Photonics* **9**, 594 (2015).
  - [14] K. Saha, Y. Okawachi, B. Shim, J. S. Levy, R. Salem, A. R. Johnson, M. A. Foster, M. R. E. Lamont, M. Lipson, and A. L. Gaeta, *Optics Express* **21**, 1335 (2013).
  - [15] P. Marin-Palomo, J. N. Kemal, M. Karpov, A. Kordts, J. Pfeifle, M. H. P. Pfeiffer, P. Trocha, S. Wolf, V. Brasch, R. Rosenberger, K. Vijayan, W. Freude, T. J. Kippenberg, and C. Koos, arXiv **1610.01484**, 13 (2016), arXiv:1610.01484.
  - [16] A. Dutt, C. Joshi, X. Ji, J. Cardenas, Y. Okawachi, K. Luke, A. L. Gaeta, and M. Lipson, arXiv **1611.07673**, 1 (2016), arXiv:1611.07673.
  - [17] M.-G. Suh, Q. Yang, K. Yang, X. Yi, and K. J. Vahala, *Science* **354**, 600 (2016).
  - [18] W. Liang, D. Eliyahu, V. S. Ilchenko, A. A. Savchenkov, A. B. Matsko, D. Seidel, and L. Maleki, *Nature Communications* **6**, 7957 (2015).
  - [19] V. Brasch, M. Geiselmann, T. Herr, G. Lihachev, M. H. P. Pfeiffer, M. L. Gorodetsky, and T. J. Kippenberg, *Science* **351**, 357 (2016).
  - [20] C. Joshi, J. K. Jang, K. Luke, X. Ji, S. A. Miller, A. Klenner, Y. Okawachi, M. Lipson, and A. L. Gaeta, *Optics Letters* **41**, 1 (2016), arXiv:1603.08017.
  - [21] X. Yi, Q.-F. Yang, K. Y. Yang, M.-G. Suh, and K. J. Vahala, *Optica* **2**, 1078 (2015).
  - [22] P.-H. Wang, J. A. Jaramillo-Villegas, Y. Xuan, X. Xue, C. Bao, D. E. Leaird, M. Qi, and A. M. Weiner, *Optics Express* **24**, 10890 (2016), arXiv:arXiv:1601.05036.
  - [23] D. J. Moss, R. Morandotti, A. L. Gaeta, and M. Lipson, *Nature Photonics* **7**, 597 (2013).
  - [24] C. Bao, L. Zhang, A. B. Matsko, Y. Yan, Z. Zhao, G. Xie,

- A. M. Agarwal, L. C. Kimerling, J. Michel, L. Maleki, and A. E. Willner, *Optics Letters* **39**, 6126 (2014).
- [25] M. H. P. Pfeiffer, A. Kordts, V. Brasch, M. Zervas, M. Geiselmann, J. D. Jost, and T. J. Kippenberg, *Optica* **3**, 20 (2016), arXiv:1511.05716.
- [26] M. H. P. Pfeiffer, J. Liu, M. Geiselmann, and T. J. Kippenberg, arXiv **1608.06607**, 1 (2016), arXiv:1608.06607.
- [27] C. Milián and D. V. Skryabin, *Optics Express* **22**, 3732 (2014).
- [28] L. A. Lugiato and R. Lefever, *Physical Review Letters* **58**, 2209 (1987).
- [29] J. Liu, V. Brasch, M. H. P. Pfeiffer, A. Kordts, A. Kamel, H. Guo, M. Geiselmann, and T. J. Kippenberg, *Optics Letters* **41**, 3134 (2016).
- [30] M. Karpov, H. Guo, A. Kordts, V. Brasch, M. H. P. Pfeiffer, M. Zervas, M. Geiselmann, and T. J. Kippenberg, *Physical Review Letters* **116**, 103902 (2016).
- [31] Q.-F. Yang, X. Yi, K. Y. Yang, and K. J. Vahala, *Optica* **3**, 1132 (2016), arXiv:1606.00954.
- [32] H. Guo, M. Karpov, E. Lucas, A. Kordts, M. H. P. Pfeiffer, V. Brasch, G. Lihachev, V. E. Lobanov, M. L. Gorodetsky, and T. J. Kippenberg, *Nature Physics* **13** (2016), 10.1038/nphys3893.
- [33] Q. Li, T. C. Briles, D. A. Westly, T. E. Drake, J. R. Stone, R. B. Ilic, S. A. Diddams, S. B. Papp, and K. Srinivasan, arXiv **1611.09229**, 16 (2016), arXiv:1611.09229.
- [34] E. Lucas, J. D. Jost, and T. J. Kippenberg, arXiv **1609.02723**, 16 (2016), arXiv:1609.02723.
- [35] T. Herr, V. Brasch, J. D. Jost, I. Mirgorodskiy, G. Lihachev, M. L. Gorodetsky, and T. J. Kippenberg, *Physical Review Letters* **113**, 1 (2014), arXiv:1311.1716.
- [36] J. E. Bowers, A. Beling, D. J. Blumenthal, A. Bluestone, S. M. Bowers, T. C. Briles, L. Chang, S. A. Diddams, G. Fish, H. Guo, T. J. Kippenberg, T. Komljenovic, E. Norberg, S. B. Papp, M. H. P. Pfeiffer, K. Srinivasan, L. Theogarajan, K. J. Vahala, and N. Volet, 2016 IEEE International Frequency Control Symposium, IFCS 2016 - Proceedings (2016), 10.1109/IFCS.2016.7546782.
- [37] T. Ideguchi, S. Holzner, B. Bernhardt, G. Guelachvili, N. Picqué, and T. W. Hänsch, *Nature* **502**, 355 (2013), arXiv:1302.2414.